



An efficient three-dimensional non-hydrostatic model for undular bores in open channels

Cite as: Phys. Fluids **33**, 127111 (2021); <https://doi.org/10.1063/5.0073241>

Submitted: 28 September 2021 • Accepted: 21 November 2021 • Published Online: 08 December 2021

Congfang Ai (艾丛芳),  Yuxiang Ma (马玉祥),  Weiye Ding (丁伟业), et al.



View Online



Export Citation



CrossMark

ARTICLES YOU MAY BE INTERESTED IN

[Grad's distribution functions-based gas kinetic scheme for simulation of flows beyond Navier-Stokes level](#)

Physics of Fluids **33**, 122007 (2021); <https://doi.org/10.1063/5.0072061>

[Graph neural networks for laminar flow prediction around random two-dimensional shapes](#)

Physics of Fluids **33**, 123607 (2021); <https://doi.org/10.1063/5.0064108>

[Acoustic particle migration and focusing in a tilted acoustic field](#)

Physics of Fluids **33**, 122006 (2021); <https://doi.org/10.1063/5.0070700>

Physics of Fluids

SPECIAL TOPIC: Flow and Acoustics of Unmanned Vehicles

Submit Today!



An efficient three-dimensional non-hydrostatic model for undular bores in open channels

Cite as: Phys. Fluids **33**, 127111 (2021); doi: [10.1063/5.0073241](https://doi.org/10.1063/5.0073241)

Submitted: 28 September 2021 · Accepted: 21 November 2021 ·

Published Online: 8 December 2021



View Online



Export Citation



CrossMark

Congfang Ai (艾丛芳),¹ Yuxiang Ma (马玉祥),^{1,a)}  Weiye Ding (丁伟业),²  Zhihua Xie (谢志华),³ 
and Guohai Dong (董国海)¹

AFFILIATIONS

¹State Key Laboratory of Coastal and Offshore Engineering, Dalian University of Technology, 116024 Dalian, China

²School of Marine Engineering Equipment, Zhejiang Ocean University, 316022 Zhoushan, China

³Hydro-environmental Research Centre, School of Engineering, Cardiff University, CF10 3AT Cardiff, United Kingdom

^{a)} Author to whom correspondence should be addressed: yuxma@dlut.edu.cn

ABSTRACT

A three-dimensional (3D) non-hydrostatic model is presented to simulate open-channel free-surface flows involving undular bores. The 3D unsteady mass conservation and momentum equations are solved using an explicit projection method in a nonstandard staggered grid. The grid system is built from a two-dimensional horizontal structured grid by adding horizontal layers. The model is validated using four typical benchmark problems, including undular bore development, an undular bore generated by a sudden discharge, and two test cases involving undular hydraulic jumps. The proposed model results are compared with experimental data and results from other models. Overall, the agreement between the proposed model results and experimental data is generally good, demonstrating the capability of the model to resolve undular bores. In addition, the non-hydrostatic pressure field under the undular free surface is revealed, and the efficiency of the proposed model is presented. It is shown that the proposed model behaves better than a volume of fluid model in terms of efficiency, because the proposed model can use fewer computational grid cells to resolve undular bores in open channels.

Published under an exclusive license by AIP Publishing. <https://doi.org/10.1063/5.0073241>

I. INTRODUCTION

It is well known that after the opening of a sluice gate or at the head of a bore, secondary free-surface undulation may be observed. This undulation causes a larger leading wave crest and can lead to significant engineering and design challenges; in addition, it cannot be reproduced by classical shallow water models with the hydrostatic pressure assumption. To obtain better insight into the evolution of undular bores, many physical experiment (Lin *et al.*, 2020a; 2020b; Montes and Chanson, 1998; Soares-Frazão and Zech, 2002a; Treske, 1994) have been conducted over a long period of time. In recent years, numerical models incorporating non-hydrostatic effects (Biscarini *et al.*, 2010; Biswas *et al.*, 2021; Bristeau *et al.*, 2011; Castro-Orgaz and Chanson, 2021; Chang *et al.*, 2014; Hatland and Kalisch, 2019; Kim and Lynett, 2011; Mohapatra and Chaudhry, 2004; Munoz and Constantinescu, 2020; Soares-Frazão and Guinot, 2008; Soares-Frazão and Zech, 2002a; Vargas-Magana *et al.*, 2021) have been developed and successfully applied to simulate undular bores. Most of them are Boussinesq-type models (Castro-Orgaz and Chanson, 2021; Chang *et al.*, 2014; Hatland and Kalisch, 2019; Kim and Lynett, 2011; Mohapatra and Chaudhry, 2004; Soares-Frazão and Guinot, 2008;

Soares-Frazão and Zech, 2002a; Vargas-Magana *et al.*, 2021), which are depth-integrated formulations and incorporate dispersive terms to account for non-hydrostatic effects. In addition, Bristeau *et al.* (2011) derived a two-dimensional vertical (2DV) non-hydrostatic Saint-Venant system and successfully simulated undular bores generated by the rapid closing of a sluice gate. With the increase in computational power, numerical models based on Navier–Stokes equations (NSE) can also be employed to predict undular bores.

When developing NSE models, one of the primary issues is to numerically capture the moving free surface. Many famous methods have been used to simulate this moving boundary, e.g., the arbitrary Lagrangian–Eulerian method (Hodges and Street, 1999), the marker and cell method (Harlow and Welch, 1965), the volume of fluid (VOF) method (Hirt and Nichols, 1981), and the level-set method (Yue *et al.*, 2003). Currently, a few NSE models (Biscarini *et al.*, 2010; Marsooli and Wu, 2014; Munoz and Constantinescu, 2020) that incorporate the VOF method to treat free surfaces have been successfully applied to simulate dam-break flows involving undular bores. However, the high computational expense of these models usually hinders their practical applications, especially for large-scale problems.

Over the past two decades, many non-hydrostatic models have been developed to simulate open-channel flows (Lee *et al.*, 2006; and Leupi *et al.*, 2009); dispersive free-surface waves (Ai *et al.*, 2011; 2019; Stelling and Zijlema, 2003; Wu *et al.*, 2010; Young *et al.*, 2009; Yuan and Wu, 2006; Zijlema and Stelling, 2005); and oceanic internal waves (Ai and Ding, 2016; Ai *et al.*, 2021; Fringer, 2006; and Lai *et al.*, 2010). Non-hydrostatic models also solve the NSE, but employ the free-surface equation to efficiently track the free-surface motion. The so-called free-surface equation is obtained by integrating the continuity equation over the water depth and applying Leibniz's rule with the kinematic boundary conditions at the impermeable bottom and the moving free surface. In contrast to VOF-based NSE models, non-hydrostatic models usually require much fewer grid cells in the vertical direction to track the free-surface motion, but they cannot address complicated free surfaces (e.g., overturning motions). As presented by Ai *et al.* (2011), Stelling and Zijlema (2003), Wu *et al.* (2010), Yuan and Wu (2006), and Zijlema and Stelling (2005), non-hydrostatic models with a few horizontal layers can accurately predict a range of short wave motions, where wave shoaling, nonlinearity, dispersion, refraction, and diffraction phenomena occur. In view of the capability of non-hydrostatic models to resolve dispersive free-surface waves, they have the potential to predict undular bores accurately and efficiently. To the best of our knowledge, no applications of three-dimensional (3D) non-hydrostatic models on the simulation of undular bores in open channels have been published.

In this paper, we propose a 3D non-hydrostatic model to simulate undular bores in open channels. The proposed model is extended from the previous non-hydrostatic model developed by Ai *et al.* (2011), which employs an explicit projection method to solve the incompressible Euler equations. Variables are defined in a novel non-standard staggered grid system, which is built from a two-dimensional (2D) horizontal structured grid, by adding some horizontal layers. The extension of the previous model is achieved by solving the 3D Reynolds-averaging NSE instead of Euler equations and employing eddy viscosity approximations. The resulting model is validated with four typical benchmark problems: undular bore development, an undular bore generated by a sudden discharge, dam-break flow over a triangular bottom sill, and dam-break flow through an *L*-shaped channel. The model results are compared with the available experimental data and other published model results. To demonstrate the model's 3D feature and the relationship between undular bores and non-hydrostatic pressures, the non-hydrostatic pressure field under the undular free surface is presented. The model's efficiency is evaluated in the final 3D test case, which is computationally demanding.

One of the major aims of this paper is to validate the proposed model's capability to resolve undular bores in open channels. Undular bores can be formed under a variety of different circumstances. For example, in open channels undular bores can be induced by a sudden increase in discharge, the failure of a dam, dam-break waves against obstacles or closed ends, underwater moving objects, etc. The validation tests covered several circumstances that lead to the formation of undular bores. However, the proposed model has the potential to simulate undular bores resulting from more varied mechanisms.

II. MATHEMATICAL MODEL

A. Governing equations

Non-hydrostatic free-surface flows are governed by the 3D Reynolds-averaging NSE for an incompressible fluid, which are based

on the conservation of mass and momentum and can be expressed as follows:

$$\frac{\partial u}{\partial x} + \frac{\partial v}{\partial y} + \frac{\partial w}{\partial z} = 0, \tag{1}$$

$$\frac{\partial u}{\partial t} + \frac{\partial u^2}{\partial x} + \frac{\partial(uv)}{\partial y} + \frac{\partial(uw)}{\partial z} = -\frac{\partial p}{\partial x} + K^h \left(\frac{\partial^2 u}{\partial x^2} + \frac{\partial^2 u}{\partial y^2} \right) + K^v \left(\frac{\partial^2 u}{\partial z^2} \right), \tag{2}$$

$$\frac{\partial v}{\partial t} + \frac{\partial(uv)}{\partial x} + \frac{\partial v^2}{\partial y} + \frac{\partial(vw)}{\partial z} = -\frac{\partial p}{\partial y} + K^h \left(\frac{\partial^2 v}{\partial x^2} + \frac{\partial^2 v}{\partial y^2} \right) + K^v \left(\frac{\partial^2 v}{\partial z^2} \right), \tag{3}$$

$$\begin{aligned} \frac{\partial w}{\partial t} + \frac{\partial(uw)}{\partial x} + \frac{\partial(vw)}{\partial y} + \frac{\partial w^2}{\partial z} \\ = -\frac{\partial p}{\partial z} + K^h \left(\frac{\partial^2 w}{\partial x^2} + \frac{\partial^2 w}{\partial y^2} \right) + K^v \left(\frac{\partial^2 w}{\partial z^2} \right) - \frac{\rho}{\rho_0} g, \end{aligned} \tag{4}$$

where *u*, *v*, and *w* are the velocity components in the horizontal *x*, *y*, and vertical *z* directions, respectively; *p* is the normalized pressure divided by a constant reference density ρ_0 ; ρ denotes the water density; and K^h and K^v are the horizontal and vertical eddy viscosities, respectively. Finally, *t* is the time and *g* is the gravitational acceleration.

Following Casulli (1999), the pressure *p* is split into its hydrostatic and non-hydrostatic components as follows:

$$p = g(\eta - z) + q, \tag{5}$$

where η is the free-surface elevation and *q* is the non-hydrostatic pressure component.

Introducing Eq. (5) into Eqs. (2)–(4) results in the following:

$$\begin{aligned} \frac{\partial u}{\partial t} + \frac{\partial u^2}{\partial x} + \frac{\partial(uv)}{\partial y} + \frac{\partial(uw)}{\partial z} \\ = -g \frac{\partial \eta}{\partial x} - \frac{\partial q}{\partial x} + K^h \left(\frac{\partial^2 u}{\partial x^2} + \frac{\partial^2 u}{\partial y^2} \right) + K^v \left(\frac{\partial^2 u}{\partial z^2} \right), \end{aligned} \tag{6}$$

$$\begin{aligned} \frac{\partial v}{\partial t} + \frac{\partial(uv)}{\partial x} + \frac{\partial v^2}{\partial y} + \frac{\partial(vw)}{\partial z} \\ = -g \frac{\partial \eta}{\partial y} - \frac{\partial q}{\partial y} + K^h \left(\frac{\partial^2 v}{\partial x^2} + \frac{\partial^2 v}{\partial y^2} \right) + K^v \left(\frac{\partial^2 v}{\partial z^2} \right), \end{aligned} \tag{7}$$

$$\begin{aligned} \frac{\partial w}{\partial t} + \frac{\partial(uw)}{\partial x} + \frac{\partial(vw)}{\partial y} + \frac{\partial w^2}{\partial z} \\ = -\frac{\partial q}{\partial z} + K^h \left(\frac{\partial^2 w}{\partial x^2} + \frac{\partial^2 w}{\partial y^2} \right) + K^v \left(\frac{\partial^2 w}{\partial z^2} \right). \end{aligned} \tag{8}$$

To account for the difference between the horizontal and vertical grid resolutions, the horizontal and vertical eddy viscosities are determined by the Smagorinsky model (Smagorinsky, 1963) and the standard *k* – ϵ model (Rodi, 1984), respectively,

$$K^h = \nu_0 + (C_s \Delta)^2 (2S_{ij} S_{ij})^{\frac{1}{2}}, \tag{9}$$

where ν_0 is the molecular viscosity, C_s is the model parameter, and $\Delta = (\Delta x \Delta y)^{1/2}$ and Δx and Δy are the grid sizes in the *x* and *y* directions, respectively. S_{ij} is the rate of strain,

$$K^v = \nu_0 + c_\mu \frac{k^2}{\varepsilon}, \tag{10}$$

where $c_\mu = 0.09$. k and ε denote the turbulent kinetic energy and dissipation rate, respectively, and are calculated by the following $k - \varepsilon$ model (Rodi, 1984):

$$\begin{aligned} & \frac{\partial k}{\partial t} + \frac{\partial(uk)}{\partial x} + \frac{\partial(vk)}{\partial y} + \frac{\partial(wk)}{\partial z} \\ &= \frac{\partial}{\partial x} \left(\frac{K^v \partial k}{\sigma_k \partial x} \right) + \frac{\partial}{\partial y} \left(\frac{K^v \partial k}{\sigma_k \partial y} \right) + \frac{\partial}{\partial z} \left(\frac{K^v \partial k}{\sigma_k \partial z} \right) + P - \varepsilon, \tag{11} \\ & \frac{\partial \varepsilon}{\partial t} + \frac{\partial(u\varepsilon)}{\partial x} + \frac{\partial(v\varepsilon)}{\partial y} + \frac{\partial(w\varepsilon)}{\partial z} \\ &= \frac{\partial}{\partial x} \left(\frac{K^v \partial \varepsilon}{\sigma_\varepsilon \partial x} \right) + \frac{\partial}{\partial y} \left(\frac{K^v \partial \varepsilon}{\sigma_\varepsilon \partial y} \right) + \frac{\partial}{\partial z} \left(\frac{K^v \partial \varepsilon}{\sigma_\varepsilon \partial z} \right) + c_{1\varepsilon} \frac{\varepsilon}{k} P - c_{2\varepsilon} \frac{\varepsilon^2}{k}, \tag{12} \end{aligned}$$

where P is the turbulence production term. The turbulence constants are $\sigma_k = 1.0$, $\sigma_\varepsilon = 1.3$, $c_{1\varepsilon} = 1.44$, and $c_{2\varepsilon} = 1.92$.

B. Boundary conditions

Boundary conditions are required at all the boundaries of a 3D domain including the free surface, the bottom, the vertical wall, and the inflow and outflow boundaries. Only one normal and two tangential components of the velocities and/or stresses need to be described at the boundaries to obtain a unique solution.

At the free surface, atmospheric pressure is exerted so that the following Dirichlet boundary condition for the non-hydrostatic pressure q is imposed:

$$q|_{z=\eta} = 0, \tag{13}$$

where η is the free-surface elevation.

The kinematic boundary condition at the moving free surface is expressed as follows:

$$w|_{z=\eta} = \frac{\partial \eta}{\partial t} + u \frac{\partial \eta}{\partial x} + v \frac{\partial \eta}{\partial y}. \tag{14}$$

For the impermeable bottom surface $z = -d(x, y)$, the shear stress components in the directions x and y , τ_{0x} and τ_{0y} are computed as follows:

$$\frac{\tau_{0x}}{\rho} = K^v \frac{\partial u}{\partial z} = \gamma_b u_b \sqrt{u_b^2 + v_b^2}, \quad \frac{\tau_{0y}}{\rho} = K^v \frac{\partial v}{\partial z} = \gamma_b v_b \sqrt{u_b^2 + v_b^2}, \tag{15}$$

where u_b and v_b are the horizontal velocities at the bottom cell; $\gamma_b = c_f \sqrt{u_b^2 + v_b^2}/h$, where $h = \eta + d$ is the water depth; and c_f is the bottom friction coefficient and is calculated from the Manning–Strickler formulation as $c_f = 0.015(k_s/h)^{1/3}$, where the roughness value k_s is calibrated based on the measured data.

The kinematic boundary condition at the impermeable bottom is expressed as follows:

$$w|_{z=-d} = -u \frac{\partial d}{\partial x} - v \frac{\partial d}{\partial y}. \tag{16}$$

Integrating Eq. (1) from the bottom surface $z = -d(x, y)$ to the free-surface η , and subsequently using Leibniz’s rule with Eqs. (14) and (16), we can obtain the following free-surface equation:

$$\frac{\partial \eta}{\partial t} + \frac{\partial}{\partial x} \int_{-d}^{\eta} u dz + \frac{\partial}{\partial y} \int_{-d}^{\eta} v dz = 0. \tag{17}$$

For the inflow boundary condition, the horizontal velocity components are determined from the inflow hydrograph. An outflow boundary condition is imposed in the form of an open boundary or flow depth. An open boundary condition is specified using a zero gradient condition for the outlet velocities. In the case of a depth boundary condition, the water depth is given, and the outlet velocities are determined from Eq. (17). Finally, for vertical walls, the impermeability condition is specified, i.e., the velocity normal to the wall is set to zero.

III. NON-HYDROSTATIC MODEL

A. Grid system

The 3D computational domain is discretized as a 2D structured horizontal grid with some horizontal layers. In this grid system, the 3D grid projection onto the horizontal plane forms a rectilinear grid system, which has a set of N_x and N_y cells in the x and y directions, respectively. In the vertical direction, a boundary fitted grid system is employed, and the domain is uniformly divided into N_z layers (namely, the number of vertical grid cells) so that the horizontal levels $z_{m+1/2}$ are computed as follows:

$$z_{m+1/2} = -d(x, y) + m[\eta(x, y, t) + d(x, y)]/N_z, \tag{18}$$

where m is the layer index.

Figure 1 shows the arrangement of variables in the grid system. i and j are the grid indices in the x and y directions, respectively. The discrete velocities, non-hydrostatic pressure, and water surface elevation are defined at staggered locations on the $x - y$ plane, while on the vertical plane ($x - z$ or $y - z$ plane), variables are stored in a nonstandard staggered way. As presented in Ai et al. (2011), such a grid arrangement allows the zero pressure boundary condition [Eq. (13)] to be easily and accurately imposed at the free surface $z = \eta(x, y)$ and renders the discretized Poisson equation for non-hydrostatic pressure corrections symmetric and positive definite; thus, it can be solved effectively using the preconditioned conjugate gradient method. The definitions for the turbulent kinetic energy k and dissipation rate ε are identical to the position of the vertical velocity component w .

B. Numerical methods

By including diffusion terms in the momentum equations, the algorithms described in Ai et al. (2011) can also be employed to solve Eqs. (1), (6)–(8), and (17). First, based on the vertical boundary-fitted coordinate system, integrating Eqs. (1) and (6)–(8) over a horizontal layer m can yields the following semi-discretized equations:

The continuity equation,

$$\frac{\partial \Delta z_m}{\partial t} + \frac{\partial(\Delta zu)_m}{\partial x} + \frac{\partial(\Delta zv)_m}{\partial y} + \omega_{m+1/2} - \omega_{m-1/2} = 0. \tag{19}$$

The horizontal momentum equations,

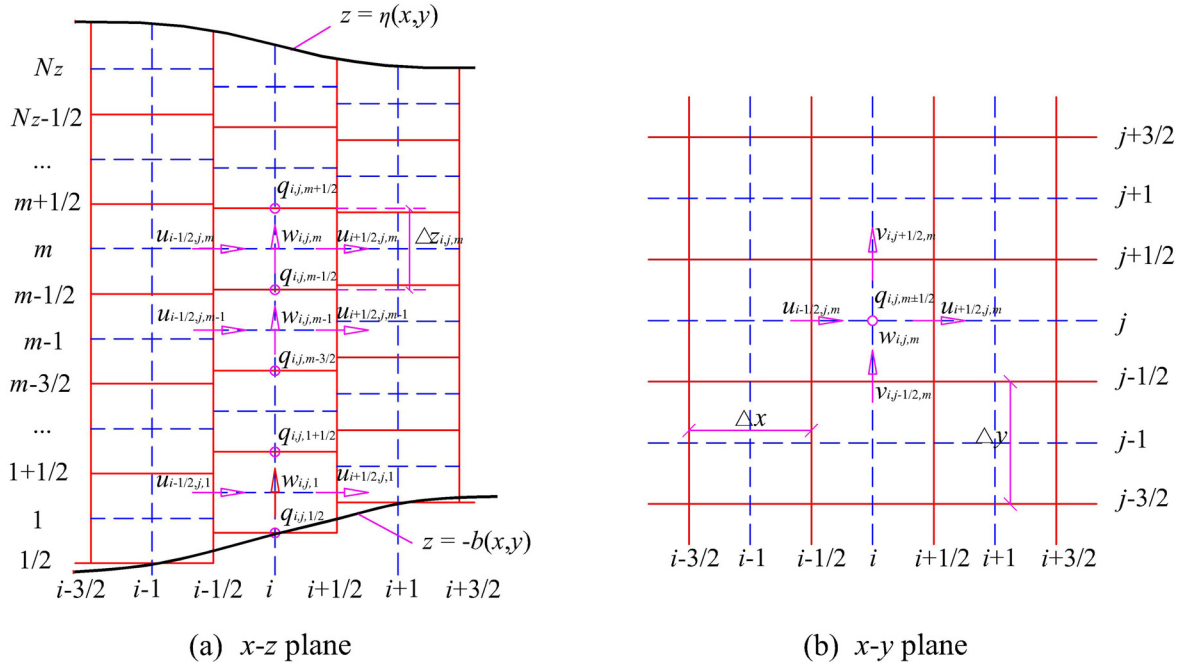


FIG. 1. Arrangement of variables in the grid system: (a) $x - z$ plane and (b) $x - y$ plane.

$$\begin{aligned} & \frac{\partial(\Delta zu)_m}{\partial t} + \frac{\partial(\Delta zuu)_m}{\partial x} + \frac{\partial(\Delta zuv)_m}{\partial y} + \omega_{m+1/2} u_{m+1/2} \\ & - \omega_{m-1/2} u_{m-1/2} + g \Delta z_m \frac{\partial \eta}{\partial x} + \Delta z_m \frac{\partial q}{\partial x} \\ & = \Delta z_m (F_u)_m + \left(K^v \frac{\partial u}{\partial z} \right)_{m+1/2} - \left(K^v \frac{\partial u}{\partial z} \right)_{m-1/2}, \end{aligned} \quad (20)$$

$$\begin{aligned} & \frac{\partial(\Delta zv)_m}{\partial t} + \frac{\partial(\Delta zvu)_m}{\partial x} + \frac{\partial(\Delta zvv)_m}{\partial y} + \omega_{m+1/2} v_{m+1/2} \\ & - \omega_{m-1/2} v_{m-1/2} + g \Delta z_m \frac{\partial \eta}{\partial y} + \Delta z_m \frac{\partial q}{\partial y} \\ & = \Delta z_m (F_v)_m + \left(K^v \frac{\partial v}{\partial z} \right)_{m+1/2} - \left(K^v \frac{\partial v}{\partial z} \right)_{m-1/2}. \end{aligned} \quad (21)$$

The vertical momentum equation,

$$\begin{aligned} & \frac{\partial(\Delta zw)_m}{\partial t} + \frac{\partial(\Delta zuw)_m}{\partial x} + \frac{\partial(\Delta zvw)_m}{\partial y} + \omega_{m+1/2} w_{m+1/2} \\ & - \omega_{m-1/2} w_{m-1/2} + q_{m+1/2} - q_{m-1/2} \\ & = \Delta z_m (F_w)_m + \left(K^v \frac{\partial w}{\partial z} \right)_{m+1/2} - \left(K^v \frac{\partial w}{\partial z} \right)_{m-1/2}, \end{aligned} \quad (22)$$

where $\Delta z_m = z_{m+1/2} - z_{m-1/2}$; F_u , F_v , and F_w represent the horizontal momentum diffusion terms; and $\omega_{m+1/2}$ is the vertical velocity ζ relative to the layer level $z_{m+1/2}$.

In the second step, Eqs. (1) and (20)–(22) are discretized by a finite difference–finite volume method and then the resulting equations are solved by an explicit projection method, which can be subdivided into two stages. The finite difference method (Ai et al., 2019;

Asghar et al., 2020; Casulli, 1999) is widely used to solve partial differential equations based on a structured grid, while the finite volume method (Ai and Ding, 2016; Fringer et al., 2006) does not require a structured grid and is usually employed to get conservative schemes. In the proposed model, the finite volume method is only used to discretize the horizontal advection terms in Eqs. (20)–(22) to achieve momentum-conserved schemes.

The first stage is to project intermediate velocities $u_{i+1/2,j,m}^{n+1/2}$; $v_{i,j+1/2,m}^{n+1/2}$; and $w_{i,j,m}^{n+1/2}$ by means of solving Eqs. (20)–(22), which contain the non-hydrostatic pressure at the previous time level. This results in the following equations:

$$\begin{aligned} u_{i+1/2,j,m}^{n+1/2} & = \text{adec}(u) + \text{diff}(u) + f_{u1} \eta_{i+1,j}^n + f_{u2} \eta_{ij}^n \\ & + f_{u3} q_{i+1,j,m+1/2}^n + f_{u4} q_{i+1,j,m-1/2}^n \\ & + f_{u5} q_{i,j,m+1/2}^n + f_{u6} q_{i,j,m-1/2}^n, \end{aligned} \quad (23)$$

$$\begin{aligned} v_{i,j+1/2,m}^{n+1/2} & = \text{adec}(v) + \text{diff}(v) + f_{v1} \eta_{i,j+1}^n + f_{v2} \eta_{ij}^n + f_{v3} q_{i,j+1,m+1/2}^n \\ & + f_{v4} q_{i,j+1,m-1/2}^n + f_{v5} q_{i,j,m+1/2}^n + f_{v6} q_{i,j,m-1/2}^n, \end{aligned} \quad (24)$$

$$w_{i,j,m}^{n+1/2} = \text{adec}(w) + \text{diff}(w) + f_{w1} q_{i,j,m+1/2}^n + f_{w2} q_{i,j,m-1/2}^n, \quad (25)$$

where f_u , f_v , and f_w are the functions of the known values at the previous time. $\text{adec}(u)$, $\text{adec}(v)$, and $\text{adec}(w)$ represent the advection terms in the corresponding momentum equations, and their finite volume discretizations can be found in Ai et al. (2011). In addition, $\text{diff}(u)$, $\text{diff}(v)$, and $\text{diff}(w)$ are discretized momentum diffusion terms that can be easily obtained using the central differencing scheme and are not provided here for brevity.

In the second stage, the new velocities $u_{i+1/2,j,m}^{n+1}$; $v_{i,j+1/2,m}^{n+1}$; and $w_{i,j,m}^{n+1}$ are computed by correcting the projected values after including

the non-hydrostatic pressure terms. Similar to Eqs. (23)–(25), expressions for $u_{i+1/2,j,m}^{n+1}$, $v_{i,j+1/2,m}^{n+1}$, and $w_{i,j,m}^{n+1}$ can be obtained as follows:

$$u_{i+1/2,j,m}^{n+1} = \text{adec}(u) + \text{diff}(u) + f_{u1}\eta_{i+1,j}^n + f_{u2}\eta_{i,j}^n + f_{u3}q_{i+1,j,m+1/2}^{n+1} + f_{u4}q_{i+1,j,m-1/2}^{n+1} + f_{u5}q_{i,j,m+1/2}^{n+1} + f_{u6}q_{i,j,m-1/2}^{n+1}, \quad (26)$$

$$v_{i,j+1/2,m}^{n+1} = \text{adec}(v) + \text{diff}(v) + f_{v1}\eta_{i,j+1}^n + f_{v2}\eta_{i,j}^n + f_{v3}q_{i,j+1,m+1/2}^{n+1} + f_{v4}q_{i,j+1,m-1/2}^{n+1} + f_{v5}q_{i,j,m+1/2}^{n+1} + f_{v6}q_{i,j,m-1/2}^{n+1}, \quad (27)$$

$$w_{i,j,m}^{n+1} = \text{adec}(w) + \text{iff}(w) + f_{w1}q_{i,j,m+1/2}^{n+1} + f_{w2}q_{i,j,m-1/2}^{n+1}. \quad (28)$$

By subtracting Eqs. (23)–(25) from Eqs. (26)–(28), we can obtain the following expressions:

$$u_{i+1/2,j,m}^{n+1} = u_{i+1/2,j,m}^{n+1/2} + f_{u3}\Delta q_{i+1,j,m+1/2} + f_{u4}\Delta q_{i+1,j,m-1/2} + f_{u5}\Delta q_{i,j,m+1/2} + f_{u6}\Delta q_{i,j,m-1/2}, \quad (29)$$

$$v_{i,j+1/2,m}^{n+1} = v_{i,j+1/2,m}^{n+1/2} + f_{v3}\Delta q_{i,j+1,m+1/2} + f_{v4}\Delta q_{i,j+1,m-1/2} + f_{v5}\Delta q_{i,j,m+1/2} + f_{v6}\Delta q_{i,j,m-1/2}, \quad (30)$$

$$w_{i,j,m}^{n+1} = w_{i,j,m}^{n+1/2} + f_{w1}\Delta q_{i,j,m+1/2} + f_{w2}\Delta q_{i,j,m-1/2}, \quad (31)$$

where $\Delta q = q^{n+1} - q^n$ is the non-hydrostatic pressure correction term.

Substitution of the expressions for $u_{i+1/2,j,m}^{n+1}$; $v_{i,j+1/2,m}^{n+1}$; and $w_{i,j,m}^{n+1}$ from Eqs. (29)–(31) into the finite difference approximation of Eq. (1) yields the Poisson equation for Δq , which can be symbolically written as follows:

$$\mathbf{A}\Delta\mathbf{q} = \mathbf{b}, \quad (32)$$

where \mathbf{A} is a symmetric and positive definite matrix with dimension $(N_x N_y N_z) \times (N_x N_y N_z)$; $\Delta\mathbf{q}$ is a vector of the calculated non-hydrostatic pressure correction; and \mathbf{b} is a known vector related to the intermediate velocities.

After the non-hydrostatic pressure correction $\Delta\mathbf{q}$ is obtained by solving Eq. (32), the new velocity field is readily determined from Eqs. (29)–(31).

In the final step, the new free-surface elevation is obtained by applying finite volume discretization to solve Eq. (17). Meanwhile, the relative velocity $\omega_{k+1/2}$ is calculated from Eq. (19), which can also be discretized using a finite volume method. More details regarding the discretization of Eqs. (17) and (19) can be found in Ai *et al.* (2011).

After the new velocities $u_{i+1/2,j,m}^{n+1}$; $v_{i,j+1/2,m}^{n+1}$; and $w_{i,j,m}^{n+1}$ and the new free-surface elevation $\eta_{i,j}^{n+1}$ are obtained, the $k - \epsilon$ model [Eqs. (11) and (12)] is solved using a discretization method similar to Eq. (8). Then, the horizontal and vertical eddy viscosities are calculated from Eqs. (9) and (10). Notably, to describe the wet–dry fronts, a novel wet–dry algorithm proposed by Ai and Jin (2012) is implemented at the beginning of each time step. Details regarding the wet–dry algorithm can be found in Ai and Jin (2012) and are not provided here for brevity. The main solution procedure is summarized in Fig. 2, in which the computational grid and the initial values of the variables are first configured at the initialization step.

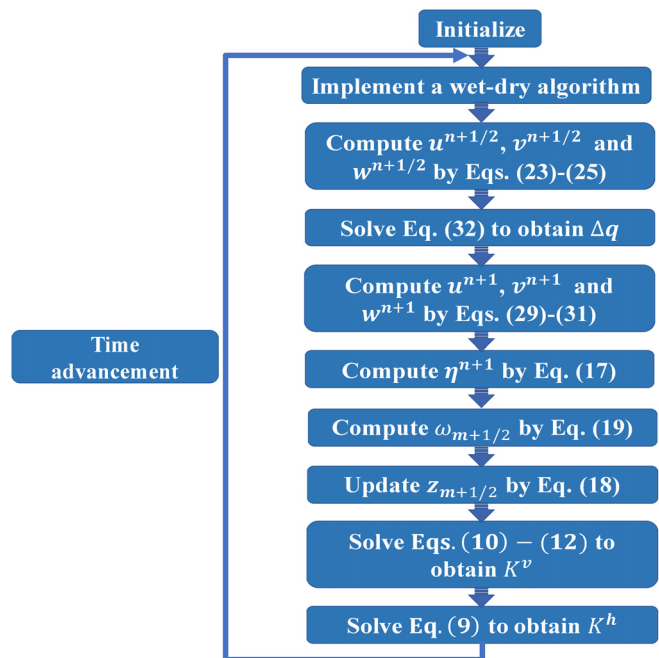


FIG. 2. Flow chart for the main solution procedure.

IV. APPLICATIONS

In this section, the proposed model’s capability is examined using four laboratory experiments involving undular bores in open channels. The former three test cases are 2DV problems, while the last case is a 3D example in which the proposed model’s efficiency is tested. In all the computations, both the horizontal grid sizes and the number of horizontal layers are specified by grid sensitivity analysis. For all the test cases, five horizontal layers are employed in the vertical direction, and C_s is taken to be 0.1.

A. Development of an undular bore

In the first example, the growth of an undular bore in a weakly non-hydrostatic system is considered. Soares-Frazão and Guinot (2008) noted that as a traveling long wave steepens, it may eventually form a bore. This process can be accurately reproduced by Boussinesq-type models (Chang *et al.*, 2014; Peregrine, 1966; Soares-Frazão and Guinot, 2008) but cannot be captured by classical shallow water models. In this study, the proposed non-hydrostatic model is used to investigate undular bore development. Following Peregrine (1966), the initial water depth and velocity field are expressed as follows:

$$h(x) = \frac{1}{g} \left[u(x)\sqrt{gh_0} + \frac{1}{4}u^2(x) \right] + h_0, \quad (33)$$

$$u(x) = \frac{1}{2}u_0\sqrt{gh_0}[1 - \tanh(x/a)], \quad (34)$$

where $h_0 = 1.0$ m is the undisturbed initial water depth; $u_0 = 0.1$ m/s is the velocity of the incoming wave; and $a = 5.0$ m is a parameter describing the shape of the incoming wave. All of the boundaries are vertical walls.

In the simulation, the initial conditions [Eqs. (33) and (34)] are specified in a flat rectangular channel, which is 120 m long in the x direction and is discretized by a grid size of $\Delta x = 0.05$ m. The origin of the x axis is located 50 m downstream of the upper end of the channel. The time step is set to 0.05 s and the roughness value is set to $k_s = 3.0 \times 10^{-4}$. Comparisons of the free-surface profiles between the two sets of Boussinesq model results, the present model results, and the measured data at four different times are plotted in Fig. 3. The Boussinesq model, which was proposed by Soares-Frazão and Guinot (2008), solves one-dimensional Boussinesq equations using a hybrid finite volume scheme with MUSCL4 reconstruction. The smooth particle hydrodynamics (SPH)-Boussinesq model employs the SPH method to solve the Lagrangian form of the 2D Boussinesq equations. The proposed model accurately reproduces the growth of the undular bore compared with the measured data and agrees well with both Boussinesq models, demonstrating the ability of the developed

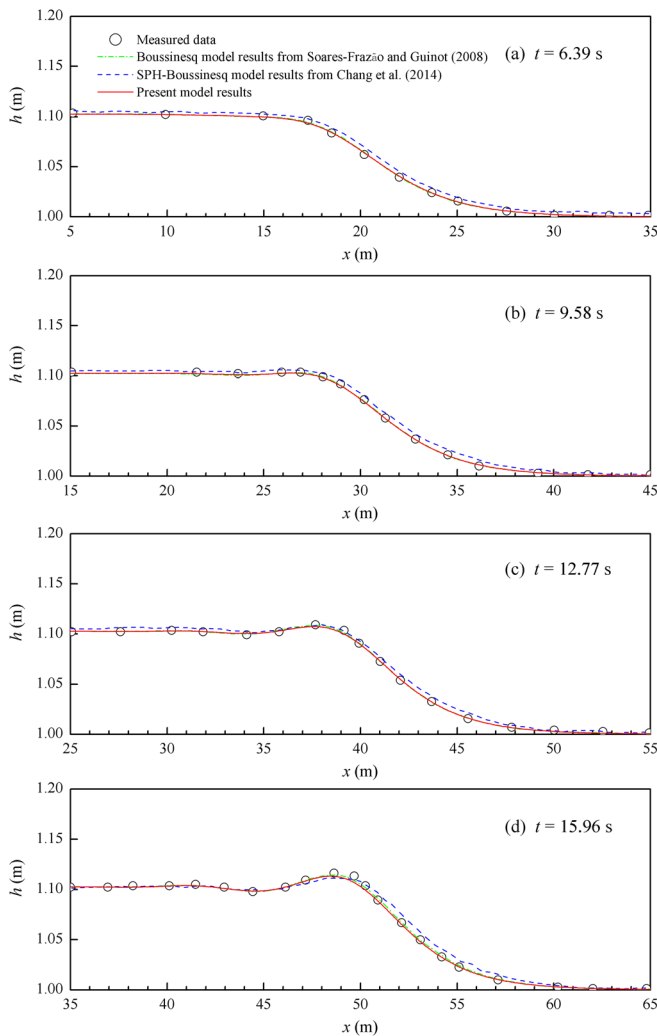


FIG. 3. Comparisons of the free-surface profile between the two sets of Boussinesq model results, the proposed model results, and the measured data at (a) $t = 6.39$ s, (b) $t = 9.58$ s, (c) $t = 12.77$ s, and (d) $t = 15.96$ s.

non-hydrostatic model to resolve undular bore development. To demonstrate the advantage of the proposed 3D model, Fig. 4 depicts the normalized non-hydrostatic pressure field obtained by the proposed model at different times. During the development of the undular bore, both the positive and negative non-hydrostatic pressure values become increasingly strong. Under the wave crest, the non-hydrostatic pressure is always negative, while a stronger and positive pressure can be observed in front of the crest.

B. Undular bore generated by a sudden discharge

Soares-Frazão and Zech (2002a) presented an experiment that investigates the formation of an undular bore generated by a sudden

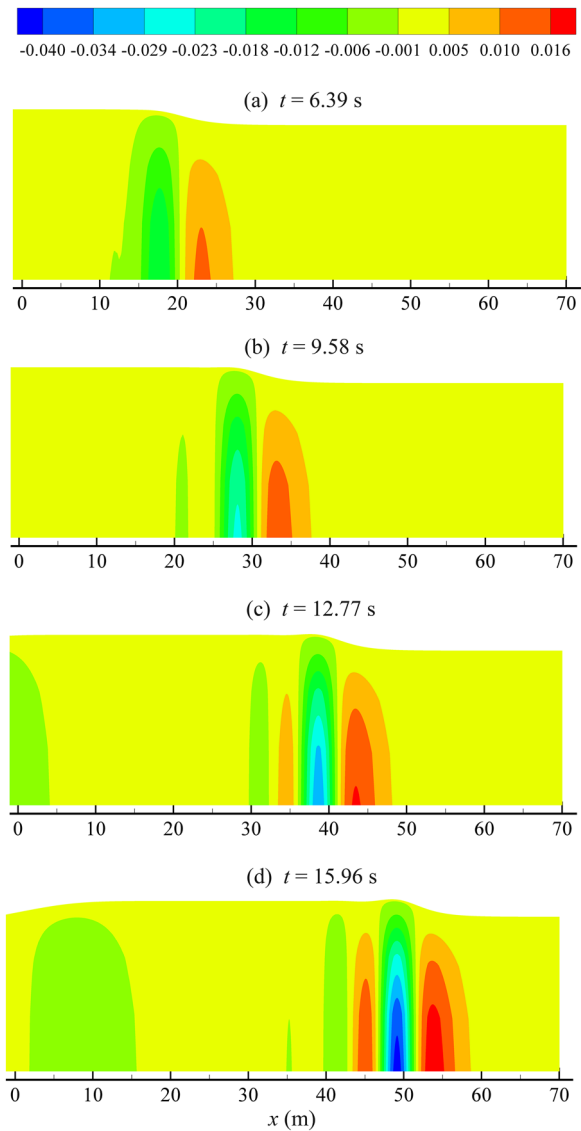


FIG. 4. The normalized non-hydrostatic pressure field q (m^2/s^2) at (a) $t = 6.39$ s, (b) $t = 9.58$ s, (c) $t = 12.77$ s, and (d) $t = 15.96$ s. (The vertical scale has been amplified by a factor of 20.)

release of water. The experiment has been widely used to validate Boussinesq-type models (Kim and Lynett, 2011; Soares-Frazão and Guinot, 2008; Soares-Frazão and Zech, 2002a). A similar test case regarding an undular bore that formed due to the closing of a sluice gate was also employed to test the 2DV non-hydrostatic Saint-Venant model proposed by Bristeau *et al.* (2011). In this study, we conduct the numerical simulation on an undular bore generated by a sudden discharge and compare the numerical results with experimental data from Soares-Frazão and Zech (2002a). Figure 5 shows a schematic view of the experiment. In the experiment, a sluice gate separates the upstream reservoir from the horizontal channel. Initially, the gate is closed and the water in both regions is at rest. The water depth in the downstream channel is 0.251 m. When the gate is opened rapidly, a bore forms and travels downstream. Following Soares-Frazão and Guinot (2008), the sudden release of the gate was modeled by imposing a unit discharge of $Q = 0.059 \text{ m}^2/\text{s}$ at the channel's upstream boundary. A constant water depth $h = 0.251 \text{ m}$ was specified at the channel's downstream boundary.

In this computation, a uniform horizontal grid size $\Delta x = 0.025 \text{ m}$ and a time step of $\Delta t = 0.02 \text{ s}$ are chosen. The roughness value k_s is set to 3.0×10^{-4} . Comparisons of the time histories of the water depth between the two sets of numerical results and the experimental data are plotted in Fig. 6. The proposed model results are quite similar to the Boussinesq model results (Soares-Frazão and Guinot, 2008) and underpredict the leading wave crest at locations C5–C1 and slightly overestimate it at location C0. However, the proposed model makes good predictions of the propagation of the leading wave crest and captures the primary feature of the undular bore generated by a sudden discharge, which is characterized by a series of solitary-like waves with gradually damping amplitudes. Figure 7 depicts the normalized non-hydrostatic pressure field obtained by the proposed model at $t = 15 \text{ s}$. The non-hydrostatic pressure varies between a positive and a negative value below the undular water surface. Moreover, as the amplitude damps, the non-hydrostatic pressure becomes weak.

C. Dam-break flow over a triangular bottom sill

When a dam-break flow encounters a bottom sill, a negative bore behind the sill will be formed and propagate upstream. Many researchers have investigated this process using laboratory experiments (Morris, 2000; Ozmen-Cagatay and Kocaman, 2011; Soares-Frazão, 2007) or numerical simulations based on VOF models (Biscarini *et al.*, 2010; Munoz and Constantinescu, 2020; Marsooli and Wu, 2014;

Ozmen-Cagatay and Kocaman, 2011). In this study, the proposed model results are compared with the experimental data published by Soares-Frazão (2007). The channel geometry and the locations of gauging points are presented in Fig. 8. The channel is 5.6 m long and the initial water depth in the 2.39 m long upstream reservoir is 0.111 m. The symmetrical triangular sill is 0.065 m high and has bed slopes of ± 0.14 . The water depth downstream of the sill is maintained at 0.02 m. Both the start and the end of the channel are vertical walls as shown in Fig. 8.

In this computation, a grid size of $\Delta x = 0.005 \text{ m}$ and a time step of $\Delta t = 0.001 \text{ s}$ are used. Three roughness values $k_s = 1.5 \times 10^{-3}$, 3.0×10^{-3} , and 6.0×10^{-3} are considered in this study. Figure 9 shows comparisons of the time histories of the water depth between the three sets of proposed model results and experimental data. Overall, the model results with $k_s = 3.0 \times 10^{-3}$ are better than those with $k_s = 1.5 \times 10^{-3}$ and 6.0×10^{-3} and are in good agreement with the experimental data. Especially at Gauging point G3, the model accurately records the propagation and reflection of several undular bores during the first 45 s after the dam break. As described in the experiment by Soares-Frazão (2007), these bores are put down to the multiple wave reflections in the channel upstream of the sill between the wall at the upstream boundary and the triangular sill. To reveal the role of non-hydrostatic pressures in the development of undular bores, the normalized non-hydrostatic pressure fields during the first 15 s are depicted in Fig. 10, in which the origin of the x coordinate is located at the upstream boundary of the channel. Figures 10(a)–10(c) show a bore that reflects against the sill and propagates upstream with a free-surface undulation, while Figs. 10(d)–10(f) show an undular bore that reflects against the upstream wall and then travels back toward the sill. The non-hydrostatic pressure also varies between positive and negative values below the undular water surface. Moreover, whether the bore propagates upstream or downstream, as the first wave amplitude damps, the non-hydrostatic pressure below becomes weak.

D. Dam-break flow through an L-shaped channel

The proposed model has been validated by three 2DV problems, so the final example is focused on a 3D test case. The dam-break experiment in an L-shaped channel, which was conducted by Soares-Frazão and Zech (2002b), is employed; this experiment has been used as a benchmark test for the validation of classical shallow water models (Gottardi and Venutelli, 2004; Liu *et al.*, 2013; Ortiz, 2014) and VOF models (Biscarini *et al.*, 2010; Munoz and Constantinescu, 2020). Kim

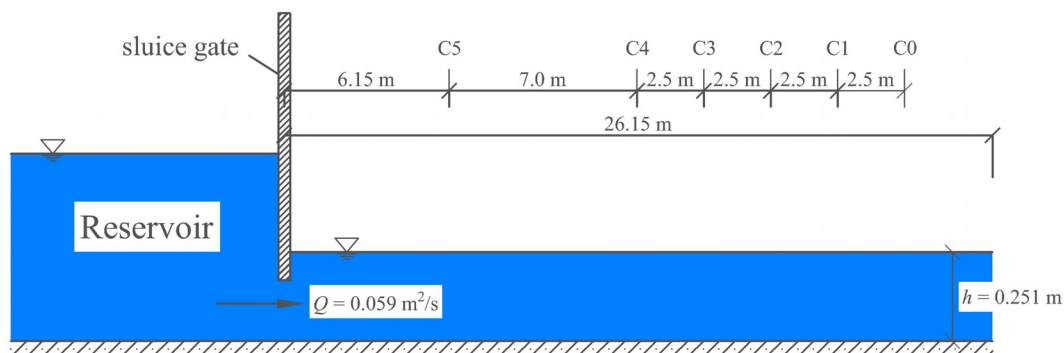


FIG. 5. Experimental setup for the undular bore generated by a sudden discharge.

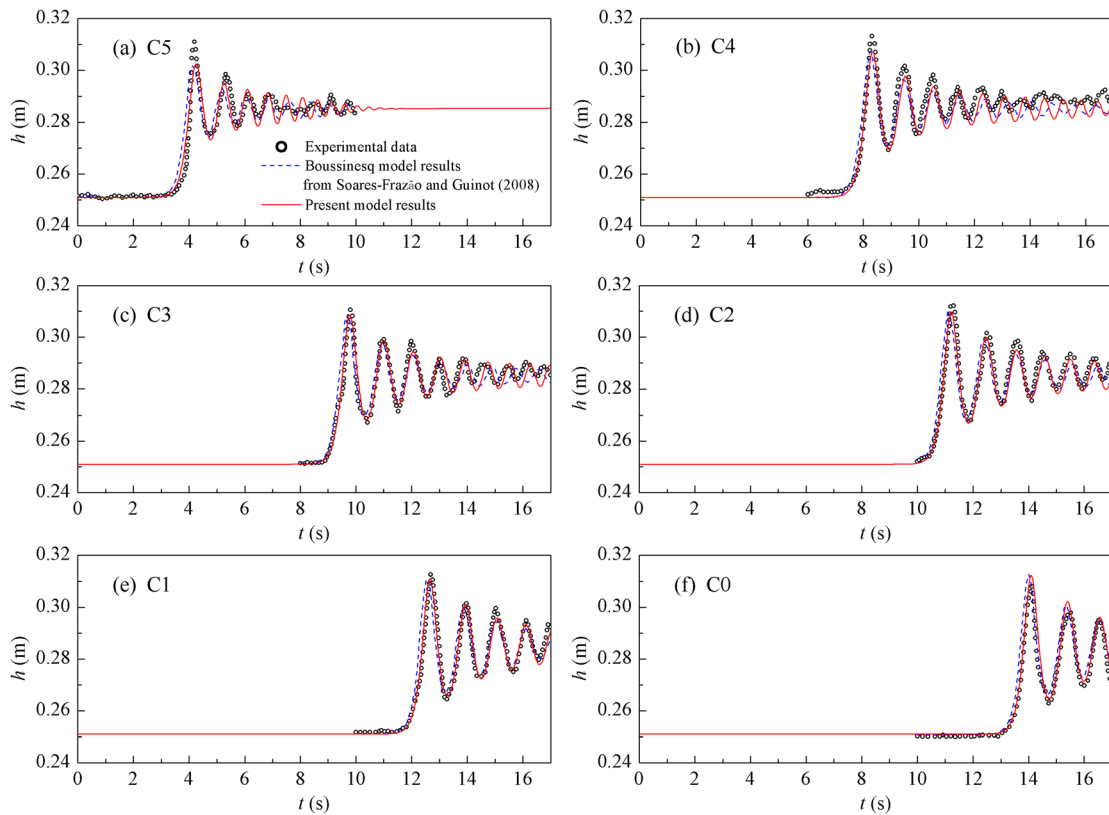


FIG. 6. Comparisons of the time histories of the water depth among the Boussinesq model results published by Soares-Frazão and Guinot (2008), the proposed model results, and the experimental data. (a) Location C5, (b) Location C4, (c) Location C3, (d) Location C2, (e) Location C1, and (f) Location C0.

and Lynett (2011) also employed a Boussinesq-type model to investigate the non-hydrostatic effects in this dam-break process.

The dam-break experiment was conducted in a domain consisting of a rectangular reservoir connected to an L-shaped channel. Both the reservoir and the channel are horizontal and connected by a dam. The geometry of the experimental layout and the locations of the gauging points are presented in Fig. 11. Following Kim and Lynett (2011), the bottom surface of the reservoir is identical to the channel bed elevation. Initially, the water depth in the reservoir is 0.2 m, and the channel is dry. All the boundaries are vertical walls except the end of the channel, which is an open boundary.

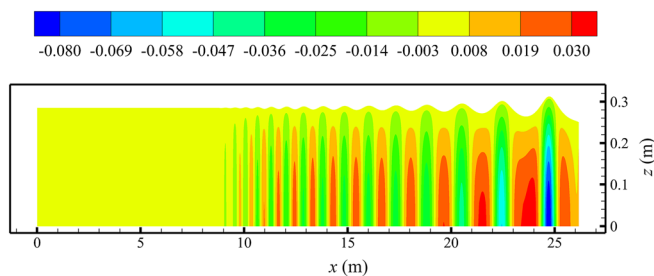


FIG. 7. The normalized non-hydrostatic pressure field q (m^2/s^2) at $t = 15$ s.

In the horizontal plane, according to an analysis of the computed results' sensitivity to the horizontal grid spacing, grid sizes $\Delta x = \Delta y = 0.01$ m are used in this computation. The total grid cells are therefore $93\,850 \times 5 = 469\,250$. The time step is set to 0.002 s, and the total simulation time is up to 40 s. The roughness value k_s is calibrated to be 3.0×10^{-3} . During the simulation time, the dam-break wave propagates toward the downstream channel and collides with the channel bend boundaries; then, a hydraulic jump forms in the bend region and propagates upstream with a free-surface undulation. Comparisons of the time histories of the water depth between the two sets of numerical results and experimental data at different gauging points are plotted in Fig. 12. The Boussinesq model results from Kim and Lynett (2011) are only available for Gauging points P2–P6. For all the gauging points, the proposed model results are similar to the Boussinesq model results and both model results are in reasonable agreement with the measured data. Both model results show a large wave crest at Gauging point P4. The reason for this crest is that wave breaking may occur when the dam break wave first encounters the channel bend boundaries and both models cannot address wave breaking accurately without the incorporation of a wave breaking algorithm.

3D view plots of the water depth, which describe the formation of the hydraulic jump and its propagation upstream into the reservoir, are illustrated in Fig. 13. At $t = 6.0$ s, the water depth in the bend increases, and a hydraulic jump gradually forms. Hereafter, the

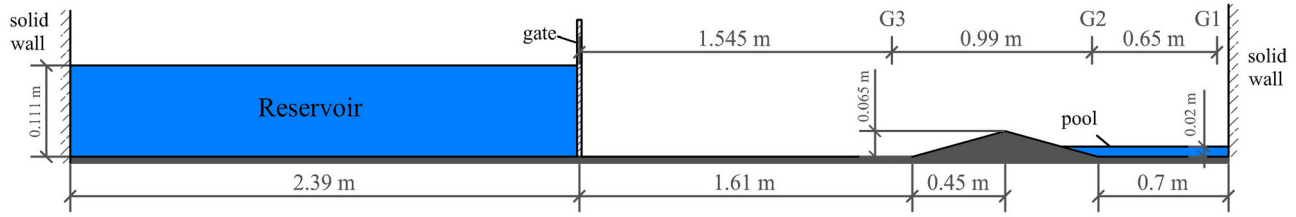


FIG. 8. Sketch of the geometry for dam-break flow over a triangular bottom sill.

hydraulic jump propagates upstream with a free-surface undulation. At $t = 17.0$ s, the undular hydraulic jump has just arrived at the reservoir.

This computation was conducted on a desktop computer with an Intel(R) Core(TM) i7-7700K CPU. The CPU is a four-core processor with a base frequency of 4.2 GHz and total RAM of 32 GB. The proposed model was implemented using C# multithread technology. The CPU time was approximately 4.8 h. In addition, Munoz and Constantinescu (2020) employed the pressure-Poisson solver (a VOF model) in STAR-CCM+ to simulate a similar test case on a four-core PC with 16 GB of RAM per core, but they used 9 000 000 grid cells to discretize the computational domain. The simulation time is 14 s, and

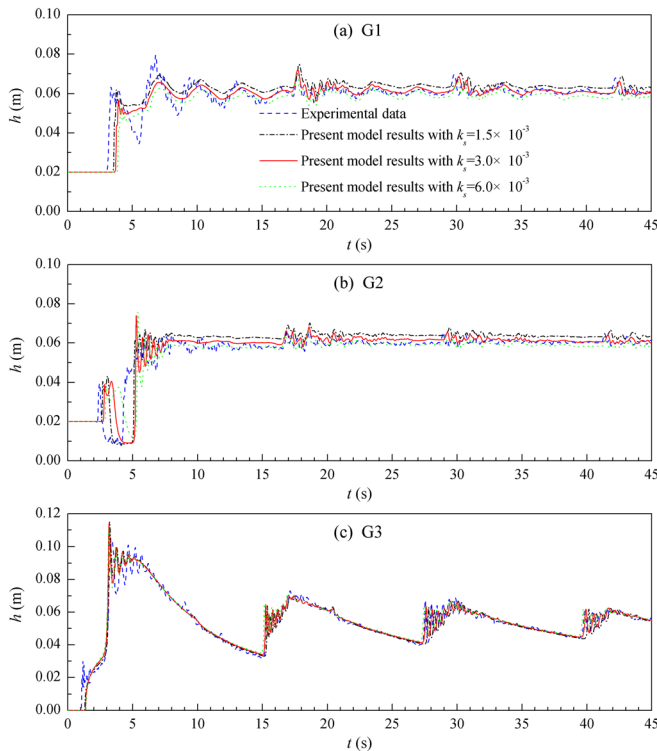


FIG. 9. Comparisons of the time histories of the water depth between the three sets of the present model results with different roughness values and measured data. (a) Gauging point G1, (b) Gauging point G2, and (c) Gauging point G3.

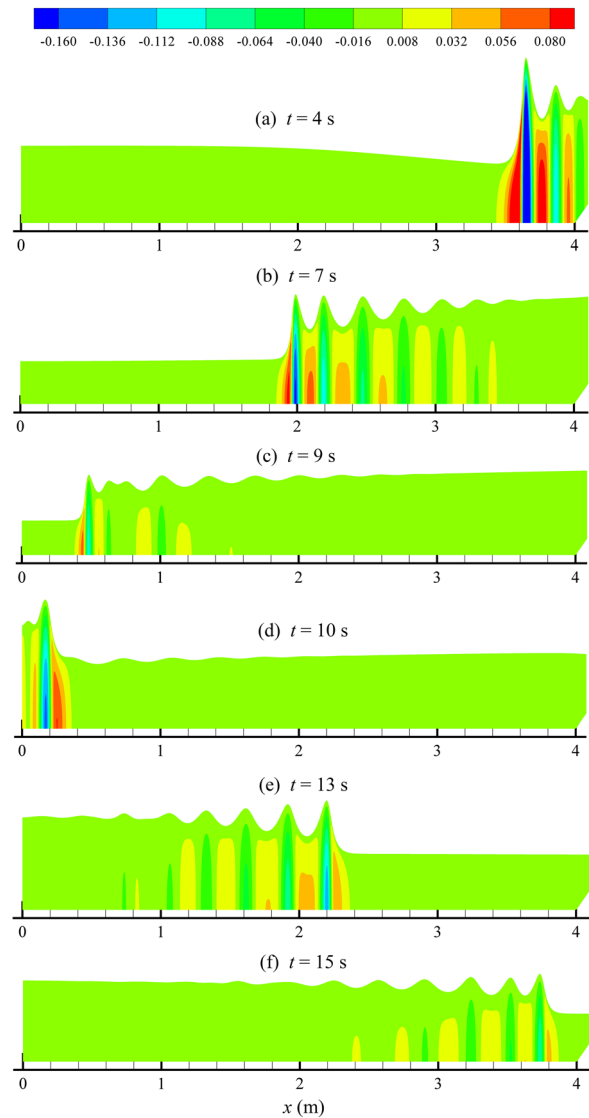


FIG. 10. Normalized non-hydrostatic pressure fields q (m^2/s^2) after the dam break at (a) $t = 4$ s, (b) $t = 7$ s, (c) $t = 9$ s, (d) $t = 10$ s, (e) $t = 13$ s, and (f) $t = 15$ s. (The vertical scale has been amplified by a factor of 10.)

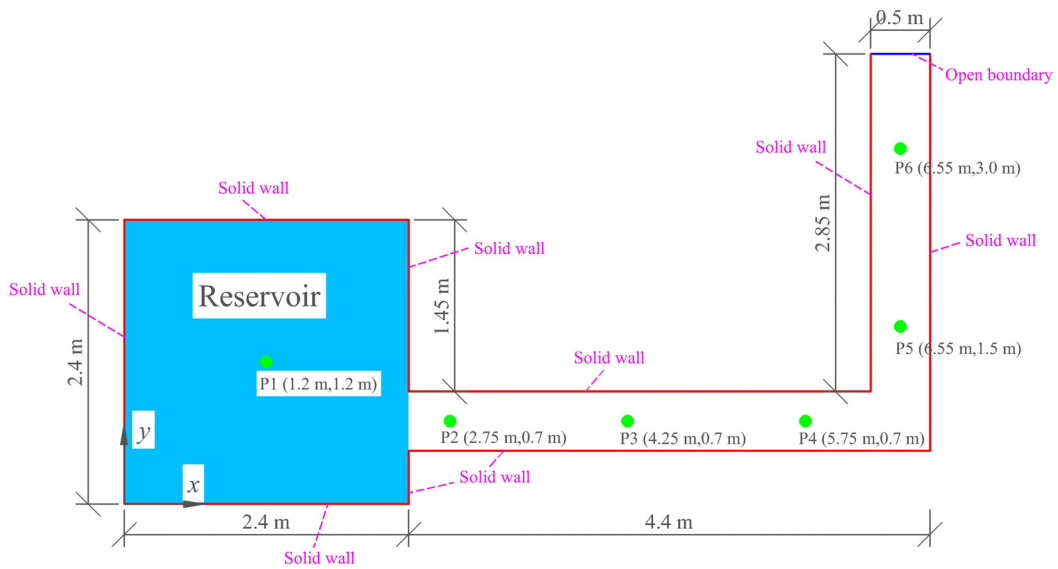


FIG. 11. The layout of the dam-break flow through an L-shaped channel.

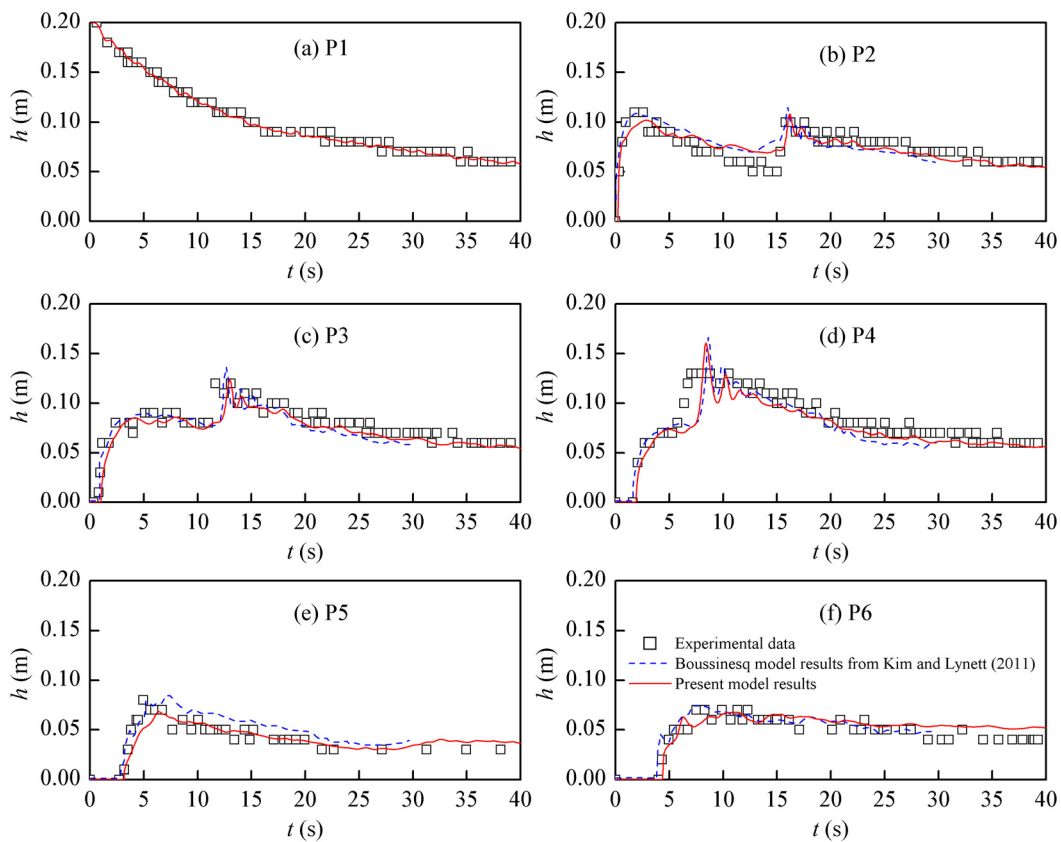


FIG. 12. Comparisons of the time histories of the water depth among the Boussinesq model results published by Kim and Lynett (2011), the present model results, and the experimental data. (a) Gauging point P1, (b) Gauging point P2, (c) Gauging point P3, (d) Gauging point P4, (e) Gauging point P5, and (f) Gauging point P6.

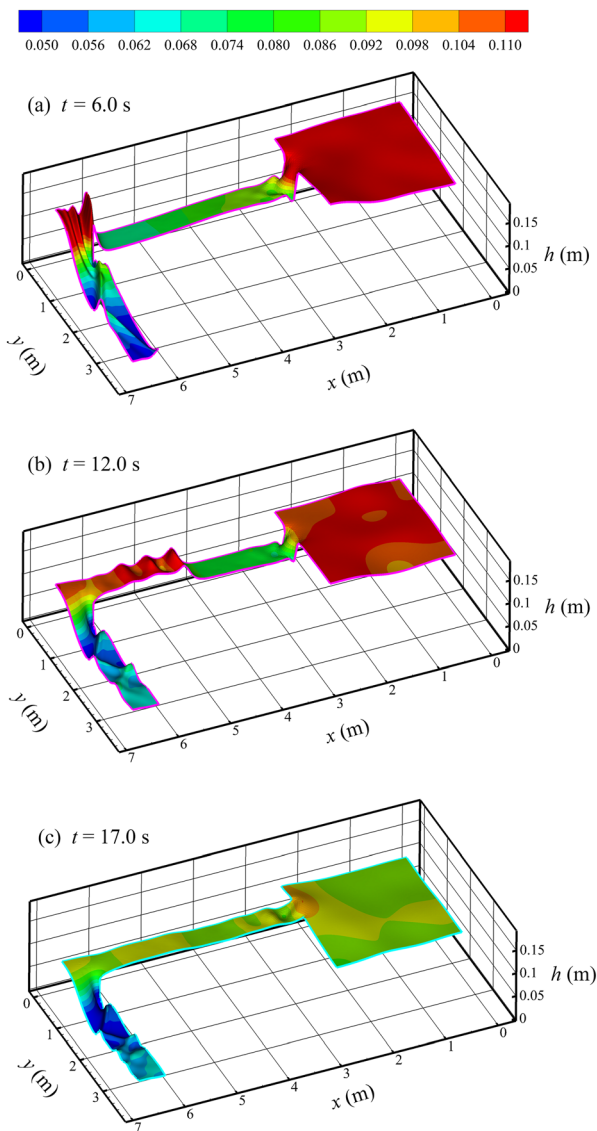


FIG. 13. 3D view plots of the water depth at different times: (a) $t = 6.0$ s, (b) $t = 12.0$ s, and (c) $t = 17.0$ s.

the corresponding CPU time for the VOF model is approximately 20 h. Notably, in a similar test case considered by Munoz and Constantinescu (2020), the reservoir's bottom surface is 0.33 m lower than the channel bed elevation, and both the size of the reservoir and channel are slightly different from those used in this study. Moreover, only the outer-bank free-surface profiles along the channel are available. Therefore, a comparison of numerical results between the proposed model and the VOF model is not provided here.

V. CONCLUSIONS

This paper proposes a 3D non-hydrostatic free-surface model that simulates undular bores in open channels. This model utilizes an

explicit projection method to solve the 3D Reynolds-averaging NSE, which are discretized using a finite difference–finite volume method in a nonstandard staggered grid. The 3D grid system is constructed from a horizontal structured grid by adding some horizontal layers. The horizontal and vertical eddy viscosities are calculated based on the Smagorinsky model (Smagorinsky, 1963) and the standard $k - \epsilon$ model (Rodi, 1984), respectively, to consider the difference between the horizontal and vertical grid resolutions. The proposed model results have been compared with available experimental data and results from other models. Generally, good agreement between the proposed model results and the experimental data has been achieved, demonstrating the capability of the proposed model to resolve undular bores in open channels.

Particularly, for the former three test cases in which wave breaking may not occur, the non-hydrostatic pressure field under the undular free surface is revealed by the proposed model. Regarding the development of an undular bore, it is found that a negative non-hydrostatic pressure is distributed below the wave crest, while in front of the crest, the non-hydrostatic pressure field is positive. Moreover, with the development of the undular bore, both the positive and negative values become increasingly strong. The undular bore generated by a sudden discharge is characterized by a series of solitary-like waves with gradually damping amplitudes. Under free-surface undulation, the non-hydrostatic pressure varies between positive and negative values, but both values become weak as the wave amplitude damps. Regarding the dam-break flow over a triangular sill, the non-hydrostatic pressure field below the undular bore is very similar to that presented in the previous test case. During the propagation of the undular bore, the first wave amplitude damps gradually and the non-hydrostatic pressure below the undular bore becomes weaker.

For the last test case, wave breaking may occur when the dam-break wave first encounters the channel bend boundaries. For this reason, the proposed model without a wave breaking algorithm predicts a larger leading wave crest at the gauging point near the channel bend boundaries. However, the proposed model accurately predicts that the hydraulic jump propagates upstream with free-surface undulation. In addition, a comparison of computational time between the proposed model and a VOF model indicates that the proposed model's efficiency may be better than that of VOF models because the proposed model can employ fewer computational grid cells to resolve undular bores in open channels.

ACKNOWLEDGMENTS

This research was supported by the National Natural Science Foundation of China (Grant Nos. 52171248, 51720105010, and 51979029), LiaoNing Revitalization Talents Program (Grant No. XLYC1807010), and the Fundamental Research Funds for the Central Universities (Grant Nos. DUT2019TB02 and DUT21LK01).

AUTHOR DECLARATIONS

Conflict of Interest

The authors have no conflicts to disclose.

DATA AVAILABILITY

The data that support the findings of this study are available from the corresponding author upon reasonable request.

NOMENCLATURE

d	bottom surface (m)
g	gravitational acceleration (m s^{-2})
i	grid index in the x direction
j	grid index in the y direction
k	turbulent kinetic energy (N m)
K^h	horizontal eddy viscosity ($\text{m}^2 \text{s}^{-2}$)
k_s	roughness value (m)
K^v	vertical eddy viscosity ($\text{m}^2 \text{s}^{-2}$)
m	grid index in the z direction
NSE	Navier–Stokes equations
N_x	number of cells in the x direction
N_y	number of cells in the y direction
N_z	number of cells in the z direction
p	normalized pressure ($\text{m}^2 \text{s}^{-2}$)
P	turbulence production term (N m s^{-1})
q	non-hydrostatic pressure component ($\text{m}^2 \text{s}^{-2}$)
S_{ij}	rate of strain (s^{-1})
t	time (s)
u	velocity component in the x direction (m s^{-1})
u_b	velocity component in the x direction at the bottom cell (m s^{-1})
v	velocity component in the y direction (m s^{-1})
v_b	velocity component in the y direction at the bottom cell (m s^{-1})
ν_0	molecular viscosity ($\text{m}^2 \text{s}^{-1}$)
VOF	volume of fluid method
w	velocity component in the z direction (m s^{-1})
$z_{m+1/2}$	layer level (m)
Δq	non-hydrostatic pressure correction term ($\text{m}^2 \text{s}^{-2}$)
Δx	grid size in the x direction (m)
Δy	grid size in the y direction (m)
Δz_m	layer thickness (m)
ε	turbulent dissipation rate
η	free-surface elevation (m)
ρ	water density (kg m^{-3})
ρ_0	constant reference density (kg m^{-3})
τ_{0x}	shear stress component in the x direction ($\text{m}^2 \text{s}^{-2}$)
τ_{0y}	shear stress components in the y direction ($\text{m}^2 \text{s}^{-2}$)
$\omega_{m+1/2}$	vertical velocity relative to the layer level $z_{m+1/2}$
2D	two-dimensional
2DV	two-dimensional vertical
3D	three-dimensional

REFERENCES

- Ai, C. and Ding, W., “A 3D unstructured non-hydrostatic ocean model for internal waves,” *Ocean Dyn.* **66**, 1253–1270 (2016).
- Ai, C. and Jin, S., “A multi-layer non-hydrostatic model for wave breaking and run-up,” *Coastal Eng.* **62**, 1–8 (2012).
- Ai, C., Jin, S., and Lv, B., “A new fully non-hydrostatic 3D free surface flow model for water wave motions,” *Int. J. Numer. Methods Fluids* **66**, 1354–1370 (2011).
- Ai, C., Ma, Y., Yuan, C., and Dong, G., “Development and assessment of semi-implicit nonhydrostatic models for surface water waves,” *Ocean Model.* **144**, 101489 (2019).
- Ai, C., Ma, Y., Yuan, C., and Dong, G., “Non-hydrostatic model for internal wave generations and propagations using immersed boundary method,” *Ocean Eng.* **225**, 108801 (2021).
- Asghar, Z., Ali, N., Waqas, M., and Javed, M. A., “An implicit finite difference analysis of magnetic swimmers propelling through non-Newtonian liquid in a complex wavy channel,” *Comput. Math. Appl.* **79**, 2189–2202 (2020).
- Biscarini, C., Francesco, S. D., and Manciola, P., “CFD modelling approach for dam break flow studies,” *Hydrol. Earth Syst. Sci.* **14**, 705–718 (2010).
- Biswas, T. R., Dey, S., and Sen, D., “Modeling positive surge propagation in open channels using the Serre-Green-Naghdi equations,” *Appl. Math. Model.* **97**, 803–820 (2021).
- Bristeau, M. O., Goutal, N., and Sainte-Marie, J., “Numerical simulations of a non-hydrostatic shallow water model,” *Comput. Fluids* **47**, 51–64 (2011).
- Castro-Orgaz, O. and Chanson, H., “Free surface profiles of near-critical instabilities in open channel flows: Undular hydraulic jumps,” *Environ. Fluid Mech.* (published online 2021).
- Casulli, V., “A semi-implicit finite difference method for non-hydrostatic, free-surface flows,” *Int. J. Numer. Methods Fluids* **30**, 425–440 (1999).
- Chang, F. J., Chang, K. H., and Kao, H. M., “A new approach to model weakly nonhydrostatic shallow water flows in open channels with smoothed particle hydrodynamics,” *J. Hydrol.* **519**, 1010–1019 (2014).
- Fringer, O. B., Gerritsen, M., and Street, R. L., “An unstructured-grid, finite-volume, nonhydrostatic, parallel coastal ocean simulator,” *Ocean Model.* **14**, 139–173 (2006).
- Gottardi, G. and Venutelli, M., “Central scheme for two-dimensional dam-break flow simulation,” *Adv. Water Resour.* **27**, 259–268 (2004).
- Harlow, F. H. and Welch, J. E., “Numerical calculation of time-dependent viscous incompressible flow of fluid with free surface,” *Phys. Fluids* **8**, 2182–2189 (1965).
- Hatland, S. D. and Kalisch, H., “Wave breaking in undular bores generated by a moving weir,” *Phys. Fluids* **31**, 033601 (2019).
- Hirt, C. W. and Nichols, B. D., “Volume of fluid (VOF) method for the dynamic of free boundaries,” *J. Comput. Phys.* **39**(1), 201–225 (1981).
- Hodges, B. R. and Street, R. L., “On simulation of turbulent nonlinear free-surface flows,” *J. Comput. Phys.* **151**(2), 425–457 (1999).
- Kim, D. H. and Lynett, P. J., “Dispersive and nonhydrostatic pressure effects at the front of surge,” *J. Hydraul. Eng.* **137**(7), 754–765 (2011).
- Lai, Z., Chen, C., Cowles, G. W., and Beardsley, R. C., “A nonhydrostatic version of FVCOM: 2. Mechanistic study of tidally generated nonlinear internal waves in Massachusetts Bay,” *J. Geophys. Res.* **115**, C12049, <https://doi.org/10.1029/2010JC006331> (2010).
- Lee, J. W., Teubner, M. D., Nixon, J. B., and Gill, P. M., “A 3-D non-hydrostatic pressure model for small amplitude free surface flows,” *Int. J. Numer. Methods Fluids* **50**, 649–672 (2006).
- Leupi, C., Miglio, E., Altinakar, M., Quarteroni, A., and Deville, M. O., “A 3D finite element model for free-surface flows,” *Comput. Fluids* **38**, 1903–1916 (2009).
- Lin, C., Kao, M.-J., Yuan, J.-M., Raikar, R. V., Hsieh, S.-C., Chuang, P.-Y., Syu, J.-M., and Pan, W.-C., “Similarities in the free-surface elevations and horizontal velocities of undular bores propagating over a horizontal bed,” *Phys. Fluids* **32**, 063605 (2020a).
- Lin, C., Kao, M.-J., Yuan, J.-M., Raikar, R. V., Wong, W.-Y., Yang, J., and Yang, R.-Y., “Features of the flow velocity and pressure gradient of an undular bore on a horizontal bed,” *Phys. Fluids* **32**, 043603 (2020b).
- Liu, Y., Zhou, J., Song, L., Zou, Q., Liao, L., and Wang, Y., “Numerical modeling of free-surface shallow flows over irregular topography with complex geometry,” *Appl. Math. Model.* **37**, 9482–9498 (2013).
- Marsooli, R. and Wu, W., “3-D finite-volume model of dam-break flow over uneven beds based on VOF method,” *Adv. Water Resour.* **70**, 104–117 (2014).
- Mohapatra, P. K. and Chaudhry, M. H., “Numerical solution of Boussinesq equations to simulate dam-break flows,” *J. Hydraul. Eng.* **130**(2), 156–159 (2004).
- Montes, J. S. and Chanson, H., “Characteristics of undular hydraulic jumps: Experiments and analysis,” *J. Hydraul. Eng.* **124**(2), 192–205 (1998).
- Morris, M., CADAM: Concerted Action on Dambreak Modeling—Final Report (HR Wallingford, Wallingford, UK, 2000).
- Munoz, D. H. and Constantinescu, G., “3-D dam break flow simulations in simplified and complex domains,” *Adv. Water Resour.* **137**, 103510 (2020).
- Ortiz, P., “Shallow water flows over flooding areas by a flux-corrected finite element method,” *J. Hydraul. Res.* **52**(2), 241–252 (2014).
- Ozmen-Cagatay, H. and Kocaman, S., “Dam-break flow in the presence of obstacle: Experiment and CFD simulation,” *Eng. Appl. Comput. Fluid Mech.* **5**(4), 541–552 (2011).

- Peregrine, D. H., "Calculations of the development of an undular bore," *J. Fluid Mech.* **25**(2), 321–330 (1966).
- Rodi, W., *Turbulence Models and Their Applications in Hydraulics*, 2nd ed. (Delft, 1984).
- Smagorinsky, J., "General circulation experiments with the primitive equations: 1. The basic experiment," *Mon. Weather Rev.* **91**(3), 99–164 (1963).
- Soares-Frazão, S., "Experiments of dam-break wave over a triangular bottom sill," *J. Hydraul. Res.* **45**, 19–26 (2007).
- Soares-Frazão, S. and Guinot, V., "A second-order semi-implicit hybrid scheme for one-dimensional Boussinesq-type waves in rectangular channels," *Int. J. Numer. Methods Fluids* **58**, 237–261 (2008).
- Soares-Frazão, S. and Zech, Y., "Dam break in channels with 90° bend," *J. Hydraul. Eng.* **128**(11), 956–968 (2002b).
- Soares-Frazão, S. and Zech, Y., "Undular bores and secondary waves experiments and hybrid finite-volume modeling," *J. Hydraul. Res.* **40**(1), 33–43 (2002a).
- Stelling, G. S. and Zijlema, M., "An accurate and efficient finite-difference algorithm for non-hydrostatic free-surface flow with application to wave propagation," *Int. J. Numer. Methods Fluids* **43**, 1–23 (2003).
- Treske, A., "Undular bores (Favre waves) in open channels—Experimental studies," *J. Hydraul. Res.* **32**(3), 355–370 (1994).
- Vargas-Magana, R. M., Marchant, T. R., and Smyth, N. F., "Numerical and analytical study of undular bores governed by the full water wave equations and bidirectional Whitham-Boussinesq equations," *Phys. Fluids* **33**(6), 067105 (2021).
- Wu, C. H., Young, C. C., Chen, Q., and Lynett, P. J., "Efficient nonhydrostatic modeling of surface waves from deep to shallow water," *J. Waterw. Port C* **136**(2), 104–118 (2010).
- Young, C. C., Wu, C. H., Liu, W., and Kuo, J., "A higher-order non-hydrostatic σ model for simulating non-linear refraction-diffraction of water waves," *Coastal Eng.* **56**, 919–930 (2009).
- Yuan, H. and Wu, C. H., "Fully nonhydrostatic modeling of surface waves," *J. Eng. Mech.* **132**, 447–456 (2006).
- Yue, W. S., Lin, C. L., and Patel, V. C., "Numerical simulation of unsteady multi-dimensional free-surface motions by level set method," *Int. J. Numer. Methods Fluids* **42**, 853–884 (2003).
- Zijlema, M. and Stelling, G. S., "Further experiences with computing non-hydrostatic free-surface flows involving water waves," *Int. J. Numer. Methods Fluids* **48**, 169–197 (2005).